

Continuation and stability of rotating waves in the magnetized spherical Couette system: Secondary transitions and multistability

F. Garcia^{1,2} and F. Stefani¹

¹ Helmholtz-Zentrum Dresden-Rossendorf
, P.O. Box 510119, D-01314 Dresden, Germany.

² Anton Pannekoek Institute for Astronomy, University of Amsterdam,
Postbus 94249, 1090 GE Amsterdam, The Netherlands.

March 9, 2024

Abstract

Rotating waves (RW) bifurcating from the axisymmetric basic magnetized spherical Couette (MSC) flow are computed by means of Newton-Krylov continuation techniques for periodic orbits. In addition, their stability is analysed in the framework of Floquet theory. The inner sphere rotates whilst the outer is kept at rest and the fluid is subjected to an axial magnetic field. For a moderate Reynolds number $Re = 10^3$ (measuring inner rotation) the effect of increasing the magnetic field strength (measured by the Hartmann number Ha) is addressed in the range $Ha \in (0, 80)$ corresponding to the working conditions of the HEDGEHOG experiment at Helmholtz-Zentrum Dresden-Rossendorf. The study reveals several regions of multistability of waves with azimuthal wave number $m = 2, 3, 4$, and several transitions to quasiperiodic flows, i.e modulated rotating waves (MRW). These nonlinear flows can be classified as the three different instabilities of the radial jet, the return flow and the shear-layer, as found in previous studies. These two flows are continuously linked, and part of the same branch, as the magnetic forcing is increased. Midway between the two instabilities, at a certain critical Ha , the nonaxisymmetric component of the flow is maximum.

1 Introduction

The origin of the magnetic fields of planets, stars and galaxies constitutes one of the most challenging problems of modern physics. Larmor was the first to suggest that the magnetic fields of the Sun, the Earth and cosmic bodies are supported by electrically conducting fluid motions in their interiors [1]. Many years later, the first successful dynamo experiments with

liquid sodium [2] supported this idea. The dynamo problem involves a large range of scales, and hence provides tremendous experimental, analytical and numerical challenges in the parameter regime relevant to geophysical and astrophysical applications. We refer to the review article [3] and a book [4] for detailed references and the history of the field.

One of the paradigms of magnetohydrodynamic flows in spherical bodies such as planets and stars is magnetized spherical Couette (MSC) flow. An electrically conducting liquid is confined between two differentially rotating spheres and is subjected to a magnetic field. Despite its simplicity, this model gives rise to a rich variety of instabilities, and it is also important from an astrophysical point of view. For instance, simulations of spherical Couette (SC) flow were used to compute the gravitational wave signal generated by global nonaxisymmetric shear flows in a neutron star [5]. In addition, instabilities observed in a liquid sodium flow between differentially rotating spheres in the presence of a magnetic field were attributed in [6] to the magnetorotational instability (MRI), but see [7, 8, 9] for alternative interpretations. Since the pioneering work of [10], MRI has been considered the best candidate to explain the mechanism of transporting angular momentum in accretion disks around black holes and stars, and also in protoplanetary disks [11], allowing matter to fall into the center. Various types of the MRI have also been studied experimentally at Helmholtz-Zentrum Dresden-Rossendorf (HZDR) [12, 13, 14].

Although the MSC represents one of the simplest paradigms of astrophysical magnetohydro-dynamics, it possesses several peculiarities that make the problem difficult. From the analytical point of view, the nonlinear nature of the Navier-Stokes equations and the spherical geometry of the boundaries lead to mathematical complications for developing analytical theories that are indeed hard to treat. For this reason, the development and improvement of appropriate numerical techniques is of key importance for a deep understanding of nonlinear flows, even in the weakly supercritical regime. In addition, thin Ekman or Ekman-Hartmann boundary layers, depending on the strength of the magnetic field, appear when the no-slip condition, used to model planetary dynamos and for comparison with laboratory experiments, is imposed at one boundary. Even in the absence of a magnetic field, [15] showed analytically the existence of a thin shear layer (Stewartson layer) at the tangent cylinder (containing the inner sphere and parallel to the rotation axis) which separates regions of different flow behavior. These thin shear layers make the numerical treatment extremely challenging because of the higher spatial resolution which is computationally most demanding.

In the absence of magnetic fields, the solutions of the SC problem including the basic flow, the first instabilities, and even turbulent states have been widely studied experimentally [16, 17], analytically [15, 18] and numerically using direct numerical simulations (DNS) [19, 20] or continuation methods [21, 22]. Many fewer numerical studies exist in which the mag-

netic field is taken into account. Most studies deal with the linear stability analysis of the basic flow, or are build on the basis of very few nonlinear solutions, and mainly rely on considering different types of boundary conditions for the magnetic field [23, 8] (insulating or conducting inner sphere allowing magnetic lines to pass), different topologies of the applied magnetic field (dipolar [8, 24], axial [6, 7, 25], or a combination of both [26]). Sophisticated tools of hydrodynamic stability theory, such as continuation techniques, are in many aspects superior to simple DNS. For instance, time integration methods are unable to obtain unstable oscillatory solutions when all the symmetries of the flow are broken. These solutions might be relevant in organizing the global dynamics [27]. Bifurcation and continuation methods have been successfully applied during the last years to a great variety of problems in the fluid dynamics context [27, 28]. Computations based on continuation of periodic orbits of nontrivial time dependence [29, 30] and even tori [31] or other invariant objects [32] have provided useful information to clarify the dynamics.

The solution (basic state) of the SC equations is unconditionally stable up to a certain critical value of the forcing parameter (the Reynolds number, Re , measuring the strength of differential rotation). Beyond this threshold an instability develops and a branch of stable or unstable solutions bifurcates and extends into a certain region of the parameter space. The appearance of multiple states in experimental flows strongly depends on the initial state [16], and in DNS the type of perturbation applied determines the type of instability or the mode that will be selected among the bifurcated solutions [20]. To get a complete picture of the skeleton of the phase space, and thus to provide a better characterization of the instabilities and the physically realizable flows, a continuation method is necessary [33, 22, 34, 30] (see [35] for a nice tutorial).

Due to the spherical geometry and rotation the SC system has $\mathcal{SO}(2)$ symmetry. Therefore, the instability of the basic flow usually gives rise to waves traveling in the azimuthal direction, i.e. rotating waves (RW), which break the axisymmetry of the basic state [36]. A secondary Hopf bifurcation results in an amplitude or shape modulation of the flow pattern, i.e. the occurrence of modulated rotating waves (MRW), which may have different types of spatio-temporal symmetries [37, 38]. In the somewhat different case of the Taylor-Couette system, several types of RW and MRW have been identified and characterized depending on their symmetry [39]. In spherical geometry Schaeffer et al. [40] have shown that the destabilization of the Stewartson layer, which is characteristic for the basic state, gives rise to a Rossby wave of fixed azimuthal wave number, travelling in the azimuthal direction due to the curvature of the boundaries. In addition, by means of fully three-dimensional simulations, [20] reported further transitions in the supercritical regime in which the original azimuthal symmetry is replaced by a so-called shift-and-reflect symmetry [41, 36]. In case of the MSC prob-

lem the existence of RW and MRW has been confirmed by experimental studies [42], and by DNS [23, 7, 8].

Addressing the influence of the applied magnetic field, [23] have shown that the axisymmetric basic state of the axially MSC problem is equatorially symmetric and remains stable for all Hartmann numbers Ha (measuring the strength of the applied magnetic field) if the Reynolds number is sufficiently small. It can be described as a strong azimuthal flow associated with a meridional recirculation. As the Reynolds number is increased, the basic state becomes unstable to non-axisymmetric perturbations. At low Hartmann number these perturbations are equatorially antisymmetric giving rise to an instability which is essentially hydrodynamic and related to a Kelvin-Helmholtz instability (KHI) of the radial jet at the equatorial plane. MSC is also \mathcal{Z}_2 , i.e, invariant by reflections with respect to the equatorial plane, but the nonlinear saturation of the radial jet instability is equatorially asymmetric. At sufficiently large Hartmann numbers the perturbations become equatorially symmetric. For small rotation rates this instability is related to a shear layer at the tangent cylinder [23, 7] while at higher rotations the instability is located at the base of the meridional return flow [7]. In this case, increasing further the Reynolds number stabilizes the basic flow [7, 43]. When holding the Reynolds number fixed, which is the approach of the present study and of the preliminary experiments performed in [9], the two types of instability are separated by a stable regime which occurs for intermediate Hartmann numbers.

Our analysis partially fills the gap between the very high Reynolds number turbulent regime reached in some of the experiments [6] and some numerical studies [24] and the low Reynolds number laminar regime in which the linear stability of the basic state has been deeply analyzed but the nonlinear saturation of the instabilities has only been studied using a few nonlinear simulations [23, 7, 43]. The use of continuation techniques allows us to obtain precise bifurcation diagrams and to determine the stability regions of RW with azimuthal wave number $m = 2, 3, 4$ in the range of $Ha \in (0, 80)$. The paper is organized as follows: In § 2 we introduce the formulation of the problem, and the numerical method used to integrate the model equations. Next, the continuation method and the basic ingredients for the stability analysis are briefly described in § 3. In § 4 the bifurcation diagrams as a function of Ha , the stability of RW and the patterns of convection are analyzed. Finally, in § 5 the paper closes with a brief summary on the results obtained.

2 The Model

Let us consider a spherical shell of inner and outer radii r_i and r_o . The outer sphere is at rest while the inner rotates at a constant angular velocity

Ω around the $\hat{\mathbf{e}}_z$ axis. The shell is filled with a homogeneous and conducting fluid of constant density ρ , dynamic viscosity μ , magnetic diffusivity λ and electrical conductivity $\sigma = 1/(\lambda\mu_o)$, where μ_o is the free-space value for the magnetic permeability.

We are interested in a comparison with laboratory experiments [9] which subject the flow to a uniform axial magnetic field $\mathbf{B}_0 = B_0 \cos(\theta)\hat{\mathbf{e}}_r - B_0 \sin(\theta)\hat{\mathbf{e}}_\theta$, θ being the colatitude and B_0 the magnetic field strength. With the use of the eutectic alloy GaInSn as the working fluid of the HEDGEHOG experiment, the inductionless approximation can be adopted. This approximation is valid in the limit of low magnetic Reynolds number $Rm = PmRe \ll 1$, which applies in the case of the HEDGEHOG experiment because of its very low magnetic Prandtl number fluid (GaInSn) with $Pm \sim O(10^{-6})$ and the moderate Reynolds numbers (inner sphere rotation rate) considered $Re \sim 10^3$.

By scaling length, time, velocity and magnetic field by $d = r_o - r_i$, d^2/ν , $r_i\Omega$ and B_0 , respectively, decomposing the magnetic field as $\mathbf{B} = \hat{\mathbf{e}}_z + Rm\mathbf{b}$ and neglecting terms $O(Rm)$, the Navier-Stokes and induction equations become

$$\partial_t \mathbf{v} + Re(\mathbf{v} \cdot \nabla) \mathbf{v} = -\nabla p + \nabla^2 \mathbf{v} + Ha^2(\nabla \times \mathbf{b}) \times \hat{\mathbf{e}}_z, \quad (1)$$

$$0 = \nabla \times (\mathbf{v} \times \hat{\mathbf{e}}_z) + \nabla^2 \mathbf{b}, \quad (2)$$

$$\nabla \cdot \mathbf{v} = 0, \quad \nabla \cdot \mathbf{b} = 0. \quad (3)$$

In this inductionless approximation the system is governed by only three non-dimensional numbers, namely the Reynolds number, the Hartmann number and the aspect ratio:

$$Re = \frac{\Omega r_i d}{\nu}, \quad Ha = \frac{B_0 d}{\sqrt{\mu_o \rho \nu \lambda}} = B_0 d \sqrt{\frac{\sigma}{\rho \nu}}, \quad \eta = \frac{r_i}{r_o}.$$

No-slip ($v_r = v_\theta = v_\varphi = 0$) at $r = r_o$ and constant rotation ($v_r = v_\theta = 0$, $v_\varphi = \sin \theta \hat{\mathbf{e}}_\varphi$) at $r = r_i$ are the boundary conditions imposed on the velocity field. For the magnetic field, insulating exterior regions are considered in accordance with the experimental setting, see [23] for more details.

The equations are discretized and integrated with the same method as described in [44] and references therein. The velocity and magnetic fields are expressed in terms of toroidal and poloidal potentials and are expanded in spherical harmonics in the angular coordinates, and in the radial direction a collocation method on a Gauss-Lobatto mesh is used. The code is parallelized in the spectral and in the physical space by using OpenMP directives. We use optimized libraries (FFTW3 [45]) for the FFTs in φ and matrix-matrix products (dgemm GOTO [46]) for the Legendre transforms in θ when computing the nonlinear terms.

For the time integration, high order implicit-explicit backward differentiation formulas (IMEX-BDF) [44] are used. In the IMEX method we treat

the nonlinear terms explicitly in order to avoid solving nonlinear equations at each time step. The Lorenz term is also treated explicitly, which may reduce the time step in comparison with an implicit treatment. However, this is not a serious issue when moderate Ha are considered, as is the case of the present study. The use of *matrix-free* Krylov methods (GMRES [47] in our case) for the linear systems facilitates the implementation of a suitable order and time stepsize control for the time integration (see [44] for details on the implementation).

3 Computation and stability of RW

The system of Eqs. (1-3) is $\mathcal{SO}(2) \times \mathcal{Z}_2$ -equivariant, $\mathcal{SO}(2)$ generated by azimuthal rotations, and \mathcal{Z}_2 by reflections with respect to the equatorial plane. According to bifurcation theory [48, 38], the first bifurcation, which breaks the axisymmetry of the basic state, is a Hopf bifurcation giving rise to a rotating wave (RW). The linear stability analysis of the basic state [43] provides the critical values Ha_c and the drifting frequencies ω_c of these non-axisymmetric instabilities as a function of Re and η .

Rotating waves, $u(r, \theta, \varphi - \omega t) = \tilde{u}(r, \theta, \tilde{\varphi})$, with $\tilde{\varphi} = \varphi - \omega t$, can be obtained efficiently by Newton-Krylov continuation methods as steady solutions of the equations written in a reference frame which is rotating with the wave, see for instance [34] for thermal convection in spherical geometries or [49] for pipe flow. In [34] RW were obtained as a zeros of a nonlinear system, requiring the use of preconditioning techniques, to accelerate the convergence of the linear solver associated to the Newton's method. In contrast, the Stokes preconditioning method used in [49] only relies on time integration of the large nonlinear system over a single time step and thus is easier to implement if a time stepping code is already available. However, as mentioned in [30], RW can also be found as periodic orbits which is the approach followed in the present study. We note this method is not as efficient in large scale $\mathcal{SO}(2) \times \mathcal{Z}_2$ -equivariant systems as those proposed in [34, 49].

Some background necessary to follow easily this section is now provided. The discretization of Eqs. (1-3) leads to a system of ordinary differential equations (ODE) of dimension $n = (2L_{\max}^2 + 4L_{\max})(N_r - 1)$, L_{\max} and N_r being the spherical harmonic truncation parameter and the number of radial collocation points, respectively. The ODE system takes the form

$$L_0 \partial_t u = Lu + B(u, u), \quad (4)$$

where u is the vector containing the spherical harmonic coefficients of the velocity potentials at the inner radial collocation points, and L_0 and L are linear operators which include the boundary conditions, L_0 being invertible. The operator L includes all the linear terms and depends on the Hartmann number Ha , which will be the control parameter of this study. The other

parameters are kept fixed to $\eta = 0.5$ and $\text{Re} = 10^3$. Therefore, $p = \text{Ha}$ and $L = L(p)$. The bilinear operator B contains the non-linear (quadratic) terms.

3.1 Continuation of RW

To study the dependence of RW, rotating at a frequency ω and with m -fold azimuthal wave number, on the parameter $p = \text{Ha}$, pseudo-arclength continuation methods for periodic orbits are used [50, 35]. These methods obtain the curve of periodic solutions $x(s) = (u(s), \tau(s), p(s)) \in \mathbb{R}^{n+2}$, s being the arclength parameter and $\tau = 2\pi/(m\omega)$ the rotation period, by adding the pseudo-arclength condition

$$m(u, \tau, p) \equiv \langle w, x - x^0 \rangle = 0,$$

where $x^0 = (u^0, \tau^0, p^0)$ and $w = (w_u, w_\tau, w_p)$ are the predicted point and the tangent to the curve of solutions, respectively, obtained by extrapolation of the previous points along the curve.

The system which determines a single solution, $x = (u, \tau, p)$ is

$$H(u, \tau, p) = \begin{pmatrix} u - \phi(\tau, u, p) \\ g(u) \\ m(u, \tau, p) \end{pmatrix} = 0, \quad (5)$$

where $\phi(\tau, u, p)$ is a solution of Eq. (4) at time $\tau = 2\pi/(m\omega)$ and initial condition u for fixed p . The condition $g(u) = 0$ is selected to fix the undetermined phase of the RW. We use $g(u) = \langle u, \partial_\varphi u_c \rangle$ where u_c is a reference solution (a previously computed solution, or a eigenfunction provided by the linear stability analysis, for instance). It is a necessary condition for $\|u - u_c\|_2^2$ to be minimal with respect to the phase (see [34]). For the computation of the inner products $\langle \cdot, \cdot \rangle$ between two functions expanded in spherical harmonics we use the definitions of [34].

To solve the large non-linear system defined by Eq. (5) we use Newton-Krylov methods. These matrix-free methods do not require the explicit computation of the Jacobian $D_{(u, \tau, p)}H(u, \tau, p)$, but only its action on a given vector. For the linear systems we use GMRES [47]. Due to the particular form of the spectrum of $D_{(u, \tau, p)}H(u, \tau, p)$ for dissipative systems, GMRES does not need preconditioning (see [50] for details).

The action of the Jacobian $D_{(u, \tau, p)}H(u, \tau, p)$ on $\delta x = (\delta u, \delta \tau, \delta p) \in \mathbb{R}^{n+2}$ is

$$\begin{pmatrix} \delta u - v(\tau) - \dot{z}(\tau)\delta\tau \\ D_u g(u)\delta u \\ D_x m(x)\delta x \end{pmatrix} \in \mathbb{R}^{n+2}.$$

Here $z(\tau), v(\tau) \in \mathbb{R}^n$ are the solutions, at time $t = \tau$, of the system

$$\begin{aligned}\partial_t z &= L_0^{-1}(L(p)z + B(z, z)), \\ \partial_t v &= L_0^{-1}(L(p)v + B(z, v) + B(v, z)) + 2p\delta p L_0^{-1}L^{(2)}z,\end{aligned}$$

with initial conditions $z(0) = u$ and $v(0) = \delta u$, with fixed p . The dependence of L on p has been assumed to be of the form $L(p) = L^{(1)} + p^2 L^{(2)}$. Each GMRES iteration will require one evaluation of the Jacobian, therefore most of the computational cost is consumed in the integration over one tentative rotation period τ of a large ODE system of dimension $2n$. An efficient time-stepping code is hence a key ingredient for a successful application of the method.

3.2 Stability of RW

Suppose a RW $(u, \tau, p) \in \mathbb{R}^{n+2}$ has been found (we recall $\tau = 2\pi/(m\omega)$). To study the stability of this periodic solution, Floquet theory is applied. Handling the full Jacobian matrix $D_u \phi(\tau, u, p)$, where $\phi(\tau, u, p)$ is the solution of Eq. (4) at time $t = \tau$ with initial condition u and for fixed p , would require a prohibitive amount of memory due the high resolution employed in the present study. Fortunately, it is enough to compute the dominant eigenvalues and eigenvectors of the map $\delta u \rightarrow D_u \phi(\tau, u, p)\delta u = v(\tau)$, with $v(\tau)$ being the solution of the first variational equation, obtained by integrating the system

$$\begin{aligned}\partial_t z &= L_0^{-1}(L(p)z + B(z, z)), \\ \partial_t v &= L_0^{-1}(L(p)v + B(z, v) + B(v, z)),\end{aligned}$$

of dimension $2n$, with initial conditions $z(0) = u$ and $v(0) = \delta u$, over a rotation period τ , with fixed p .

The eigenvalues of the map with larger modulus, which correspond to the dominant Floquet multipliers, are computed by using the ARPACK package. RW with dominant Floquet multipliers with modulus larger (smaller) than $+1$ are unstable (stable). Note that in this problem, for any value of p , there is a marginal $(+1)$ Floquet multiplier due to the invariance under azimuthal rotations, with associated eigenfunction $v_1 = \partial_t u$. To avoid unnecessary computations it can be deflated by computing the eigenvalues of the map $\delta u \rightarrow v(\tau) - \langle v(\tau), v_1 \rangle v_1$. This method to determine the stability of the solutions is very robust but computationally expensive because it requires the time integration of an ODE system of dimension $2n$ over one rotation period. Because the periodic orbit is a RW there is a more efficient alternative to this procedure [34, 51] which consist of studying the stability as a fixed point of a vector field. Matrix transformations could be used (real shift invert, Cayley, etc.) to extract the right-most eigenvalues of the associated eigenvalue problem. Preconditioning techniques, readily available

N_r	L_{\max}	m	Eq. sym	Ha	ω	$ \lambda $	$\text{Arg}\lambda$	n
40	84	3	0	3.1316477	139.3432	1.0463643	2.4932338	563472
60	126	3	0	3.1316477	138.9097	1.0502121	2.5010735	1903104
40	84	4	1	27.327395	71.12972	0.9079801	2.2812436	563472
60	128	4	1	27.327395	71.12765	0.9080306	2.2811844	1963520

Table 1: Spatial discretization study. Frequency ω and dominant complex Floquet multiplier, $\lambda = |\lambda|e^{i\text{Arg}\lambda}$, as function of the number of radial collocation points N_r and the spherical harmonics truncation parameter L_{\max} . The total number of degrees of freedom of the system $n = (2L_{\max}^2 + 4L_{\max})(N_r - 1)$ is also shown.

from the spatial discretization, are used to accelerate the convergence of the iterative solver.

3.3 Validation of the results

Throughout the study several numerical tests, that we summarise in the following, have been performed to validate the results. For the continuation of the waves as well as the computation of its stability the fixed step time integration is checked with an VSVO implicit method and very low tolerances (see [44] for details on the time integration methods). Moreover, changing tolerances, Krylov dimension or number of desired eigenvalues when dealing with Arnoldi methods (ARPACK) helps to identify changes of stability. An initial random seed is integrated over several rotation periods before calling the eigenvalue solver. This improves the convergence to the dominant eigenfunctions by filtering spurious modes [52]. In addition, the spatial resolution is changed from time to time to look for discretization errors, see table 1. On this table, the values of the drifting frequency and the modulus and argument of the dominant Floquet multiplier are shown for two different solutions belonging to the equatorially asymmetric and symmetric regions, respectively. Errors below 1% are obtained when increasing the resolution from $N_r = 40$, $L_{\max} = 84$ to $N_r = 60$, $L_{\max} = 128$. Notice that for the higher resolution the number of degrees of freedom rises to nearly 2×10^6 . Although DNS studies of this problem have been carried out for resolution as high as $N_r = 60$ and $L_{\max} = 120$ (with $m_{\max} = 30$) (see [7]), continuation studies of MHD flows in rotating spherical shells have only reached $N_r = 36$ and $L_{\max} = 36$ spectral discretization parameters (see the very recent study [53] where dynamo rotating waves have been obtained).

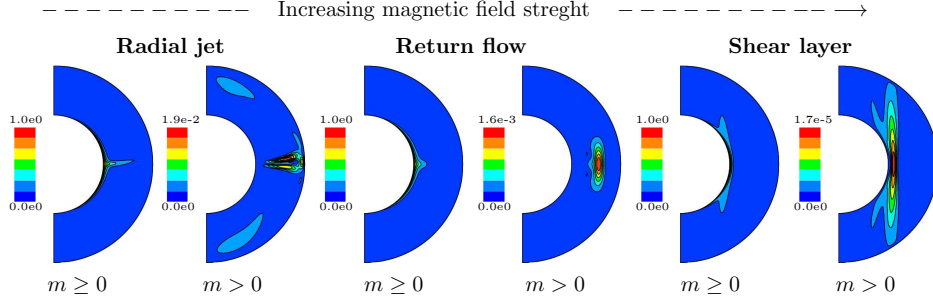


Figure 1: Contour plots of the radial jet ($\text{Ha} = 4.32$), return flow ($\text{Ha} = 29$) and shear layer ($\text{Ha} = 79.4$) instabilities. For each instability meridional sections (through a relative maximum) of $\mathbf{v}^2/2$ and its nonaxisymmetric component ($m > 0$) are shown.

4 Results

This study constitutes a further step towards the modelling of the HEDGE-HOG experiment [25, 9]. This study is restricted to $\eta = 0.5$ and $\text{Re} = 10^3$ and $\text{Ha} \in (0, 80)$ for which some experimental data is available [9]. For this range of parameters the linear stability analysis of the basic axisymmetric state has already been performed in [43]. At $\text{Re} = 10^3$ and without magnetic field ($\text{Ha} = 0$) the basic state is unstable to equatorially antisymmetric non-axisymmetric perturbations developing the radial jet instability [20]. This instability, with azimuthal wave number $m = 3$, is maintained by increasing magnetic strength, but the basic state restabilises again at a critical Hartmann number $\text{Ha}_c = 12.2$ (see Table 3. [43]). By increasing Ha further beyond $\text{Ha}_c = 25.8$ another Hopf bifurcation gives rise to a RW, with $m = 4$ and equatorially symmetric, which corresponds to the the return flow instability [7]. The return flow instability is characterised by a meridional circulation from the equatorial plane in the middle of the shell. At sufficiently large Ha the flow instabilities become magnetically confined within the tangential cylinder and strong shear layers develop [23]. This is the so-called shear-layer instability. Figure 1 exhibits the essential features of the radial jet, return flow and shear layer nonlinear instabilities with azimuthal symmetry $m = 2$. For the radial jet the nonaxisymmetric ($m > 0$) flow is concentrated near the outer boundary and very close to the equatorial plane. In the case of return flow the $m > 0$ flow is mainly developed in the bulk of the shell, at low latitudes. For the shear layer the $m > 0$ flow elongates on the axial direction, reaching high latitudes, and it is attached to the inner sphere.

The bifurcation diagrams, i.e branches of RW, for the three types of instabilities previously described are presented in the following. Azimuthal wave numbers $m = 2, 3, 4$ are selected because they are preferred at the

onset of the instabilities at aspect ratio $\eta = 0.5$ and $\text{Re} = 10^3$ [43]. They are indeed in concordance with those that can be measured with ultrasonic Doppler velocimetry (UDV) probes mounted on the HEDGEHOG experiment [9]. We also describe the flow topology of the instabilities and report the regions of multistability of the waves and the critical Hartmann numbers for the secondary bifurcations to quasiperiodic flows. The symmetry of the latter is identified and some examples, for both equatorially symmetric and antisymmetric instabilities, are provided.

4.1 Bifurcation Diagrams

Figure 2 contains the branches of RW with azimuthal wave numbers $m = 2, 3, 4$ versus the Hartmann number Ha , each panel displaying a different quantity. We recall that a $m = m_d$ nonlinear RW has an m_d -fold az-

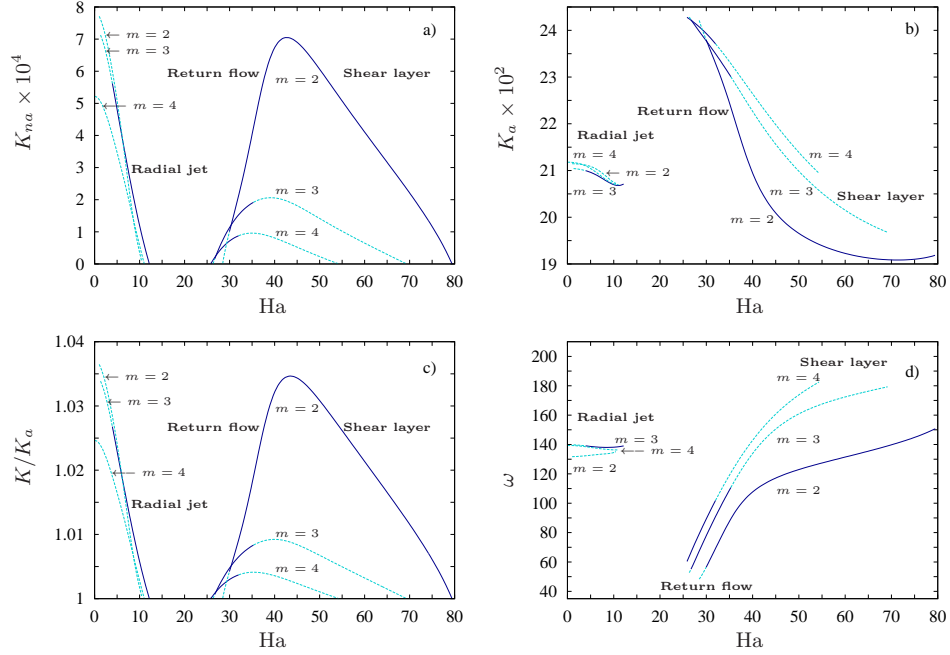


Figure 2: Bifurcation diagrams varying Ha at fixed Reynolds number $\text{Re} = 10^3$ and aspect ratio 0.5 for several time and volume averaged properties. (a) nonaxisymmetric kinetic energies K_{na} . (b) axisymmetric kinetic energies K_a . (c) Ratios of global to axisymmetric energies K/K_a . (d) Rotation frequency. Solid/dashed lines mean stable/unstable waves. The type of instability is labelled in each panel. The radial jet instability (on the left, low Ha) is equatorially asymmetric while the return flow or shear layer instabilities (on the right, moderate and high Ha) are symmetric.

imuthal symmetry (invariance under $2\pi/m_d$ azimuthal rotations) and has nonzero spherical harmonic amplitudes only for the azimuthal wave numbers $m = km_d$, $k \in \mathbb{Z}$. Volume-averaged nonaxisymmetric K_{na} and axisymmetric K_a kinetic energies, and the ratio of total over axisymmetric volume-averaged kinetic energy K/K_a , are represented in Fig. 2(a), (b), and (c), respectively. Finally, the rotation frequency ω is shown in Fig. 2(d). In all the panels, the branches of RW on the right correspond to the return flow and shear-layer instabilities, both equatorially symmetric, and those on the left correspond to the radial jet instability which is equatorially asymmetric. Unstable/stable RW are denoted with a dashed/solid line. The general picture of the situation is best displayed in Fig. 2(a) (also (c)). Each branch bifurcates from the axisymmetric basic state (horizontal axis, $K_{na} = 0$) at $\text{Ha}_c^{\text{radial jet}}(m)$, $\text{Ha}_c^{\text{return flow}}(m)$ and $\text{Ha}_c^{\text{shear layer}}(m)$ with $\text{Ha}_c^{\text{radial jet}}(m) < \text{Ha}_c^{\text{return flow}}(m) < \text{Ha}_c^{\text{shear layer}}(m)$. The azimuthal wave numbers giving rise to the critical values are $m = 3$, $m = 4$ and $m = 2$, respectively, representative of the radial jet, return flow and shear-layer instabilities. As commented before $\text{Ha}_c^{\text{radial jet}}(m = 3) = 12.2$, $\text{Ha}_c^{\text{return flow}}(m = 4) = 25.8$ (see [43]) and we have found $\text{Ha}_c^{\text{shear layer}}(m = 2) = 79.4$. According to bifurcation theory, RW bifurcating at these critical values are stable, otherwise are unstable, i.e if they bifurcate from nondominant eigenfunctions.

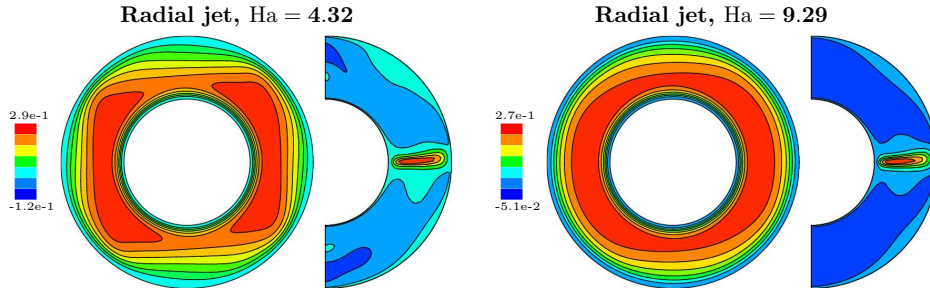


Figure 3: Contour plots of equatorially asymmetric rotating waves, corresponding to the radial jet instability, on the $m = 2$ branch. The left two plots are the equatorial and meridional sections (through a relative maximum) of radial velocity v_r at $\text{Ha} = 4.32$. Right two plots: Same sections for $\text{Ha} = 9.29$.

At the weakly magnetised regime $\text{Ha} < 12.2$, corresponding to the radial jet instability, only the $m = 3$ RW is found stable. All waves are characterised by a pronounced increase of nonaxisymmetry along the whole branch but at different rates (the smaller the value of m the larger the rate), although solutions are still nearly axisymmetric when $\text{Ha} = 0$ (see Fig. 2(c)). The difference between kinetic energies or frequencies of the branches is not so large, especially at $\text{Ha} \in (5, 12.2)$ and K_a and ω vary smoothly with Ha . The characteristic flow topology of these radial jet instabilities, exhaustively

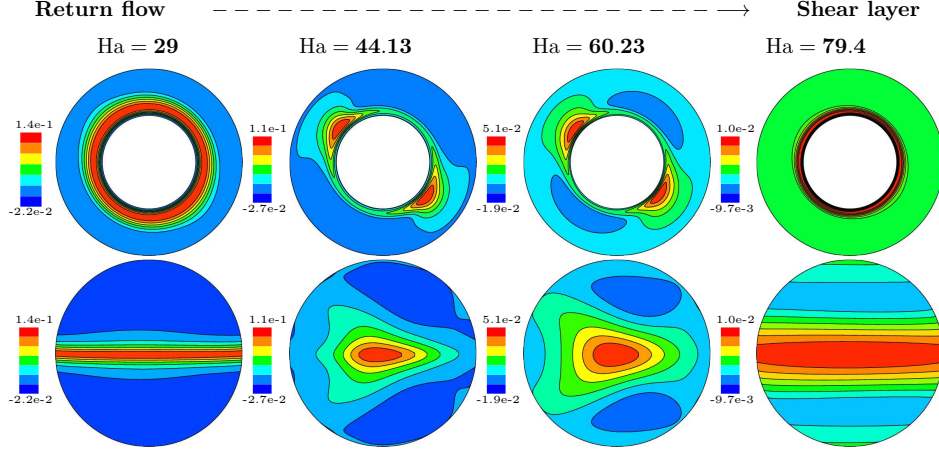


Figure 4: Contour plots of equatorially symmetric $m = 2$ RW showing the continuous transformation from the return flow to the shear-layer instability with increasing Ha . Equatorial (first row) and spherical (through a relative maximum, second row) sections of radial velocity v_r .

described in [20], can be seen in Fig. 3. Figure 3 displays a equatorial and meridional section of the radial velocity v_r (1st and 2nd plots, from left to right) for a RW with $m = 2$ azimuthal wave number and $Ha = 4.32$. The same sections are on the right group of two plots but for the $m = 2$ RW at $Ha = 9.29$. The flow results in an equatorial radial jet which emerges from the inner boundary. The flow's meridional circulation is enhanced when the radial jet reaches the outer boundary. Because of the drifting nature of the nonaxisymmetric flow the time evolution of the pattern is seen as an oscillation of the jet around the equatorial plane. The larger the non-axisymmetric component (i.e the smaller Ha), the higher latitudes the flow can affect (compare meridional sections of v_r in Fig. 3). The study of the location of convection is important from an experimental point of view since it helps to decide on the optimal position of measurement probes.

An equatorially symmetric (return flow instability) $m = 4$ RW emerges at $Ha = 25.8$ (see Fig. 2(a)). This is quite close to $Ha = 26.3$, corresponding to the bifurcation of the $m = 3$ RW. Then, a double-Hopf bifurcation similar to that described in [34] for a thermal convection in spherical geometry problem could be found by moving a second parameter (Re or η). At $Ha = 28.5$ the remaining $m = 2$ RW branch starts. Because the unstable $m = 2$ and $m = 3$ RW become stable very soon, especially in the case of $m = 3$ RW, several regions of multistability arise. They correspond to the return flow instability and will be accurately computed in § 44.2. From the beginning of the return flow instability K_{na} and ω increase sharply whilst K_a decreases for all the branches. In contrast to what occurred in the radial jet instability, the differences between K_{na} or K_a of the $m = 2, 3, 4$ branches start to rise

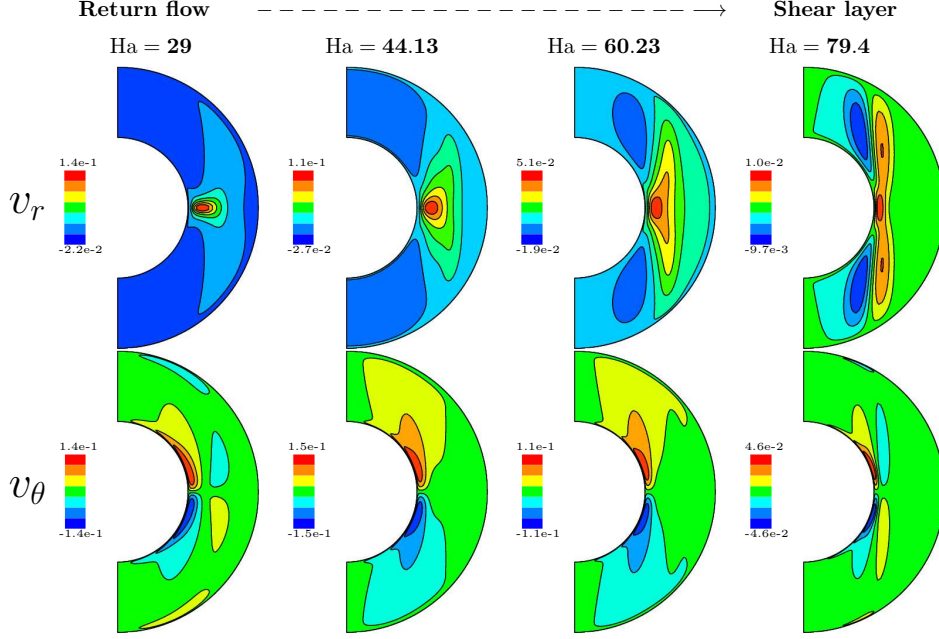


Figure 5: Contour plots of equatorially symmetric $m = 2$ RW showing the continuous transformation from the return flow to the shear-layer instability with increasing Ha . Meridional sections (through a relative maximum) of the radial v_r (first row) and colatitudinal v_θ (second row) velocities are shown.

significantly for $Ha > 30$. The same applies to the difference between ω values for $Ha > 40$. Detecting these differences is of experimental relevance because it helps to select the proper azimuthal wave number (that with a maximum signal) and thus guide in the measurement design, by positioning accordingly the UDV.

The return flow instability of the basic state turns gradually, by increasing Ha , into the shear-layer instability [7]. This also occurs when nonlinear effects are included giving rise to equatorially symmetric RW. For each m , the branch starts and ends at the basic state. Hence there is some Ha^* which maximises K_{na} as shown in Fig. 2(a). We have found that close to this Ha^* the instability can no longer be strictly classified as return flow or shear-layer because it contains features of both. Then, it seems reasonable to consider this Ha^* as the critical Hartmann number defining the boundary between return flow and shear-layer instabilities. Notice in Fig. 2(a) that Ha^* can be defined for each branch, i.e., $Ha^* \equiv Ha^*(m)$. According to our results $Ha^*(m_1) > Ha^*(m_2)$ and $K_{na}^{\max}(m_1) > K_{na}^{\max}(m_2)$ provided that $m_1 < m_2$ (the maximum value of the nonaxisymmetric kinetic energy in each branch m is $K_{na}^{\max}(m)$). Then, the smaller the value of m the larger the value of $K_{na}^{\max}(m)$ which again is interesting for experimental purposes: Nonaxisymmetric signals ($m > 0$) may be maximised by choosing properly Ha close to

$\text{Ha}^*(m)$. In addition, mounting sensors to measure low azimuthal wave number properties may also give rise to a larger signal. The existence of this critical Ha^* separating two different flow behaviours can also be inferred from the frequency dependence seen in the branches of Fig. 2(d). Approximately at Ha^* there is a change of slope (best seen for $m = 2$), indicating that frequencies change smoothly when shear-layer instabilities are selected.

Figure 2(a) shows that the smaller the m the larger is the corresponding equatorially symmetric branch. This is in correspondence with the shape of the marginal stability curves corresponding to the basic state shown in Fig. 4 of [43]. Looking at this figure and comparing with Fig. 2(a) we could imagine the $m = 5$ and $m = 6$ branches of RW to lie just below the $m = 4$ branch having both very small K_{na} . On the other hand, because all branches terminate at the basic state, Fig. 2(b) provides some information about the basic axisymmetric flow. This figure shows how the amplitude of the axisymmetric flow is increased from radial jet to return flow instability but is strongly decreased when shear-layer instabilities are selected at the higher Ha .

The features of the equatorially symmetric RW described above can be better visualised with the help of contour plots. The first row of Fig. 4 displays the contour plots of the radial velocity v_r on the equatorial plane for a sequence of $m = 2$ RW with increasing Hartmann number (from left to right $\text{Ha} = 29$, $\text{Ha} = 44.13$, $\text{Ha} = 60.23$, and $\text{Ha} = 79.4$). The left and right equatorial sections correspond to the return flow and shear-layer instabilities, respectively. The equatorial sections in between show the continuous transformation between both instabilities and the corresponding increase and decrease of the amplitude of nonaxisymmetric flow. Spherical sections (at constant r) of v_r are given in the 2nd row. Their radial positions correspond to those of the maximum, $r = r_i + \alpha d$ with $\alpha = 0.2, 0.19, 0.15, 0.12$ (from left to right). For the return flow instability the position of maximum v_r becomes fairly constant (three left spherical sections, $\text{Ha} < 45$) and increasing Ha results in a wider radial jet which spreads to higher latitudes. Beyond $\text{Ha}^* \approx 45$ the RW should be classified as shear-layer instability. The radial jet is progressively stretched to the inner boundary reaching higher latitudes. A view of the meridional sections of radial v_r and colatitudinal v_θ velocity of Fig. 5 (1st and 2nd rows, respectively), completes the picture of the transformation of return flow into the shear-layer instability. Again the sections cut a maximum of each component of the velocity. The stretching of the return flow instability is clearly seen on the sections of v_r (first row). The latter also depicts the development of strong shear layers, and the progressive alignment of the flow with the rotation axis, when the corresponding instability is selected (right sections, $\text{Ha} > 45$). The sections of v_θ (2nd row) confirm this tendency. For the shear-layer instability the strong magnetic field inhibits convection outside the tangent cylinder (parallel to the rotation axis and tangent to the inner sphere). This is because

the fluid in this region is only coupled with the outer boundary which is at rest whereas within the tangent cylinder the fluid is affected also by the inner moving boundary.

4.2 Stability Analysis: Transition to Quasiperiodic Flows

According to bifurcation (Floquet) theory a periodic orbit is stable for a given Ha as long as all its Floquet multipliers $\lambda_k \in \mathbb{C}$ lie within the unit circle $|\lambda_k| < 1$, $k = 1, \dots, n$. When, by varying Ha , one of these multipliers crosses the unit circle the periodic orbit becomes unstable. That multiplier gives information about the type of bifurcation and the type of solutions of the branch emerging at the critical point. For instance if $\lambda = \lambda_r + i\lambda_i$ is real ($\lambda_i = 0$) then a pitchfork or period doubling bifurcation, giving rise to periodic orbits of the same or twice the period of the RW, respectively, occurs depending on whether $\lambda_r = 1$ or $\lambda_r = -1$, respectively. If by contrast λ is a complex eigenvalue with $\lambda_i \neq 0$ the bifurcation is of Hopf type and the new solution branch is an invariant torus, i.e, a quasiperiodic orbit with two frequencies. The quasiperiodic scenario is found in all branches of RW, either equatorially asymmetric or symmetric.

In the absence of a magnetic field, $Ha = 0$, the critical Reynolds number is around $Re_c \approx 489$ (see [20]). Because we have chosen a significantly supercritical Reynolds of $Re = 10^3$, rotating waves with $Ha \sim 0$ are expected to be unstable. This is what occurs in the $m = 2, 3, 4$ branches of radial jet instability which have several multipliers outside the unit circle. Because of the stabilising effect of the magnetic field the unstable multipliers eventually cross the unit circle giving rise to Hopf bifurcations. In the case of $m = 2$ or $m = 4$ RW there is always one unstable multiplier whereas the $m = 3$ RW stabilises at $Ha_c = 3.95$ until the critical Hartmann for the basic state is reached ($Ha = 12.2$). At the critical parameter $Ha_c = 3.95$ the azimuthal symmetry of the eigenfunction is $m = 1$ (i.e invariant by 2π azimuthal rotations) (see Table 2) and then a branch of modulated rotating waves MRW with azimuthal symmetry $m = 1$ is born. Whether MRW are stable or not depends on whether the bifurcation is subcritical or not. It also depends on whether the parent RW state from which the MRW bifurcates is stable or not. MRWs bifurcating from unstable RWs will also be unstable. We have found that the bifurcation is subcritical and then MRW are stable with $Ha \lesssim Ha_c$. An example of MRW obtained with DNS will be shown later on. In addition, for $Ha \lesssim 3.33$ the $m = 3$ RW's have a 2nd unstable eigenfunction with azimuthal symmetry $m = 3$ (invariant to $2\pi/3$ azimuthal rotations). Then, at $Ha_c = 3.33$ an unstable branch of MRW with azimuthal symmetry $m = 3$ is born. Detecting the existence of this branches is important for a deeper understanding of temporal chaotic flows in the range $Ha \in [0, 5]$.

For all $Ha < 12.2$ explored the $m = 2$ RW's are unstable with dominant

m	Tran.	Ha_c	ω	$Arg(\lambda)$	Azim. symm.	m
2	(+, -) to (+, +)	9.43	133.82	0.10		2
3	(+, -) to (-, -)	3.95	139.07	0.77		1
4	(+, -) to (+, +)	9.97	136.08	1.49		1
4	(+, +) to (+, -)	9.98	136.08	3.13		2

Table 2: Critical parameters of the asymmetric (radial jet) RWs at the bifurcations where they change the stability ($|\lambda| = 1$). These parameters are obtained by inverse interpolation with a polynomial of degree 5. Transitions are denoted by Tran. The sign of the Floquet exponent of the two dominant eigenfunctions before and after the transition is shown. The azimuthal symmetry ($2\pi/m$ azimuthal periodicity) of the eigenfunction with a change of sign is also stated.

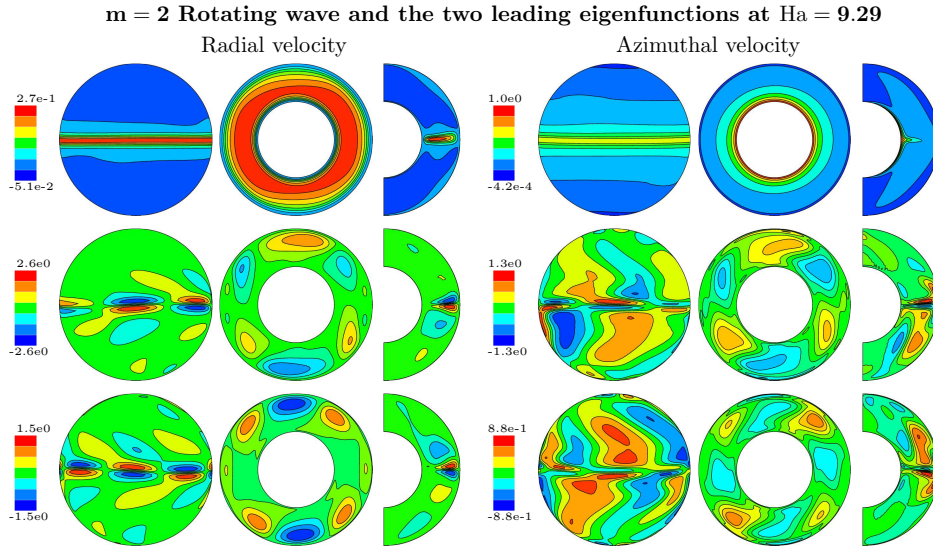


Figure 6: Contour plots of an $m = 2$ unstable equatorially asymmetric rotating wave (first row) and its two dominant eigenfunctions (second and third rows) at $Ha = 9.29$ corresponding to the radial jet instability. First row: the left three plots are the spherical, equatorial and meridional sections of the radial velocity v_r . Spherical and meridional sections are taken where v_r has a relative maximum. Right three plots: Same sections for v_ϕ . The spherical section is at $r = r_i + 0.1d$ and the meridional section cuts a relative maximum. Second/third row: As first row but for the first/second dominant eigenfunctions, respectively. In this case the spherical and meridional sections are taken at a relative maximum.

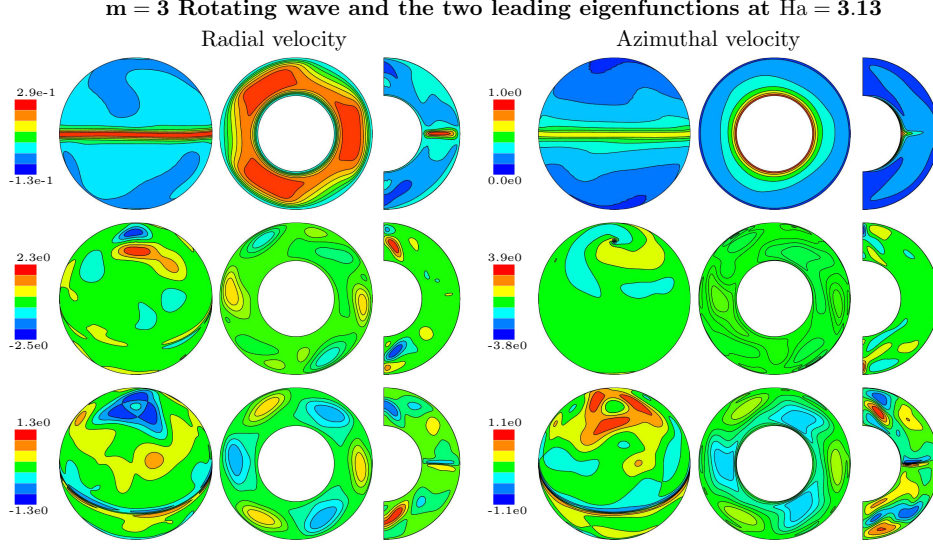


Figure 7: As Fig. 6 but for an $m = 3$ RW at $Ha = 3.13$.

eigenfunction with azimuthal symmetry $m = 1$. At $Ha \gtrsim 9.43$ the $m = 2$ RW's have a 2nd unstable eigenfunction with azimuthal symmetry $m = 2$ (invariant to $2\pi/2$ azimuthal rotations) and thus a branch of unstable MRW with azimuthal symmetry $m = 2$ could be found near this range. Since these MRW retain the $m = 2$ symmetry they can be found with $m = 2$ azimuthally constrained DNS. A similar behaviour is found for the $m = 4$ RW. For $Ha \lesssim 9.98$ they are unstable with an eigenfunction with azimuthal symmetry $m = 2$. In addition, for $Ha \gtrsim 9.97$ the $m = 4$ RW's are unstable with an eigenfunction with azimuthal symmetry $m = 1$. Then, for $Ha \in (9.97, 9.98)$ the $m = 4$ RW have two unstable eigenfunctions, while for Ha barely outside of this interval RW's have only one unstable eigenfunction. We estimate $Ha \approx 9.98$ to be the locus of a double-Hopf bifurcation.

Figures 6, 7, and 8 display the patterns (radial and azimuthal velocity) of RW and their dominant eigenfunctions lying on the $m = 2$, $m = 3$ and $m = 4$ branches, respectively. The values of Ha are selected close to bifurcation points. While the patterns of the different m RW remain quite similar, those of the eigenfunctions appear to be noticeably different. For small magnetic forcings $Ha < 5$ the instability giving rise to MRW is mainly concentrated within the tangent cylinder, i.e, in the polar regions, see Fig. 7 corresponding to a $m = 3$ RW at $Ha = 3.13$. Because these $m = 3$ RW are equatorially asymmetric and their dominant eigenfunction has azimuthal symmetry $m = 1$, the bifurcated MRW will have all the spatial symmetries broken. In the context of convection in spherical shells these solutions are quite rare and have been never reported before. In contrast, for larger values of Ha the instabilities lie closer to the outer surface in the equatorial plane.

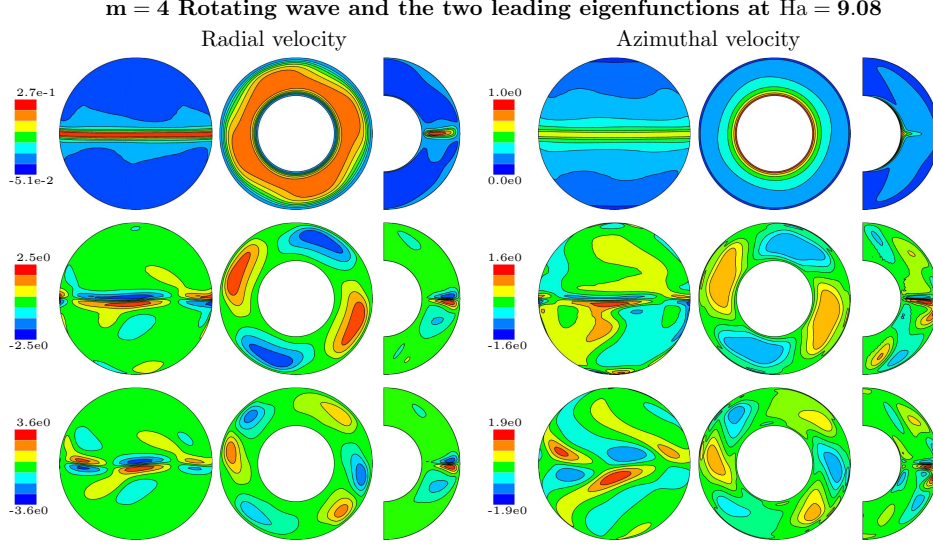


Figure 8: As Fig. 6 but for an $m = 4$ RW at $Ha = 9.08$.

Nevertheless, the instability also affects higher latitudes as it reflects the spherical sections of v_φ shown in Figs. 6 and 8, with the $m = 2$ instabilities being the most altered in this region.

The stability analysis of the return flow and shear-layer type equatorially symmetric RW, summarised in table 3, reveals several regions of multistability. These regions are displayed in Fig. 9. By means of DNS explorations we have found that the Hopf bifurcation where $m = 4$ RW lose the stability is supercritical. Then, there exists a small interval to the right of 31.95 over which an MRW is stable giving rise to a region of tri-stability (the thinner

m	Tran.	Ha_c	ω	$\text{Arg}(\lambda)$	Azim. symm. m
2	(+, -) to (-, -)	30.04	56.83	0.31	1
3	(-, -) to (-, -)	26.68	54.98	2.52	1
3	(-, -) to (+, -)	35.24	110.36	2.83	1
4	(-, -) to (+, -)	31.95	101.62	2.077	1

Table 3: Critical parameters of the symmetric RWs at the bifurcations where they change the stability ($|\lambda| = 1$). These parameters are obtained by inverse interpolation with a polynomial of degree 5. Transitions are denoted by Tran. The sign of the Floquet exponent of the two dominant eigenfunctions before and after the transition is shown. The azimuthal symmetry ($2\pi/m$ azimuthal periodicity) of the eigenfunction with a change of sign is also stated.

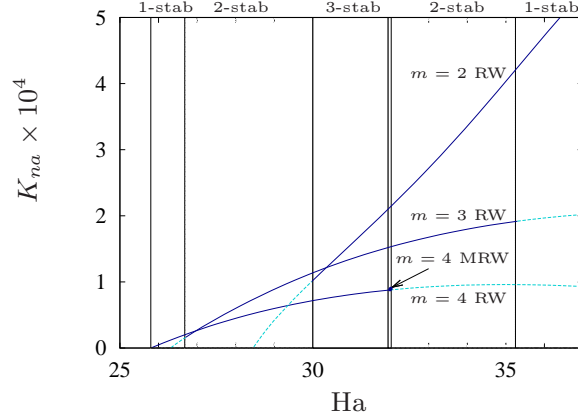


Figure 9: Bifurcation diagram varying Ha at fixed Reynolds number $Re = 10^3$ and aspect ratio 0.5 showing the time and volume averaged nonaxisymmetric kinetic energies K_{na} for the return flow instabilities. Solid/dashed lines mean stable/unstable waves. The different regions of multistability are highlighted with bands: one stable solution (cross-hatched), bi-stability (small cross-hatched) and tri-stability (solid). The narrow region corresponds to the stability region of MRW.

solid yellow band of Fig. 9). The eigenfunctions at the bifurcation point have $m = 1$ azimuthal symmetry and so do the bifurcated MRW. This also occurs at the bifurcations on the $m = 2$ and $m = 3$ branches.

The RW and their dominant eigenfunction patterns close to the bifurcation points of table 3, from top to bottom, are displayed in Fig. 10. They are all representative of return flow instability because the bifurcations occur at relatively moderate magnetic forcings $Ha < 45$. In all the cases the eigenfunctions are equatorially symmetric and the instability is concentrated in the bulk of the shell, specifically located on the edge of the radial jet. Notice that although the azimuthal symmetry is $m = 1$, in the case of $m = 2$ and $m = 4$ branches the eigenfunctions satisfy some additional symmetry, namely, they are invariant under azimuthal rotations of π degrees and change of sign. This does not occur on the $m = 3$ branch where the azimuthal symmetry is strictly $m = 1$, i.e only invariant under 2π azimuthal rotations.

As previously mentioned we have found, by means of time-stepping the model equations close to their bifurcation points, two branches of stable MRW. Specifically, one of those branches bifurcates subcritically from the equatorially asymmetric $m = 3$ RW at $Ha = 3.95$, characteristic of the radial jet instability, and the other bifurcates supercritically from the equatorially symmetric $m = 4$ RW at $Ha = 31.95$, characteristic of the return flow instability. Our explorations with DNS suggest that the interval of stability

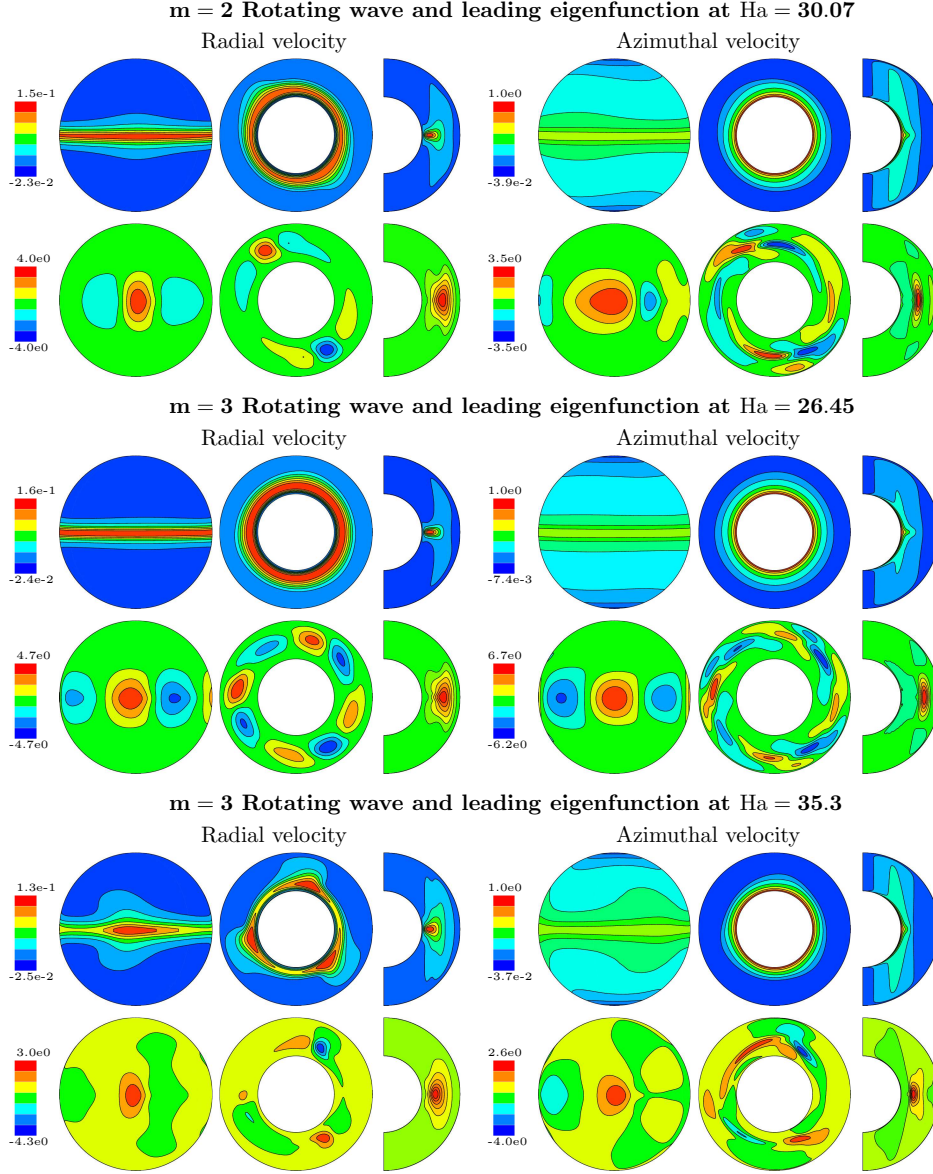


Figure 10: Contour plots of $m = 2, 3, 4$ equatorially symmetric rotating waves and their dominant eigenfunctions close to bifurcation points corresponding to the return flow instability. For each m the left three plots are the spherical, equatorial and meridional sections of the radial velocity v_r and the right three plots are the same sections for v_ϕ .

of these MRW is quite small and because of this very long initial transients are required to saturate the instability, even with initial conditions that are very close to the final state. This makes finding MRW by means of DNS quite challenging and this is why very few MRW, have been reported previously

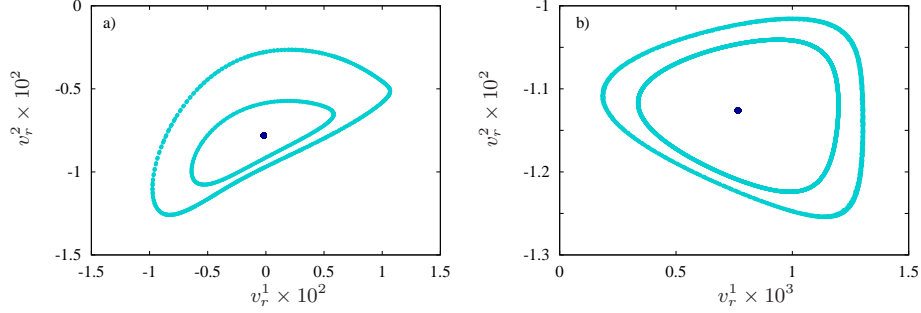


Figure 11: Poincaré sections of the radial jet and return flow instabilities (a) The Poincaré section is defined by $v_r(r_s, \theta_s, \varphi_s) = 0$, with $(r_s, \theta_s, \varphi_s) = (1.5, 3\pi/4, 0)$. Invariant tori at $\text{Ha} = 3.80$ (inner closed curve) and at $\text{Ha} = 3.54$ (outer closed curve) bifurcated from the $m = 3$ asymmetric branch. The inner point corresponds to a stable $m = 3$ periodic orbit at $\text{Ha} = 4.19$. (b) The Poincaré section is defined by $v_r(r_s, \theta_s, \varphi_s) = 0$, with $(r_s, \theta_s, \varphi_s) = (1.854, 5\pi/8, 0)$. Invariant tori at $\text{Ha} = 32$ (inner closed curve) and at $\text{Ha} = 32.02$ bifurcated from the $m = 4$ symmetric branch. The inner dot corresponds to a stable $m = 3$ periodic orbit at $\text{Ha} = 31.9$. The axis are defined by $v_r^i = v_r(r_i, \theta_i, \varphi_i)$, $i = 1, 2$ with $(r_1, \theta_1, \varphi_1) = (1.5, 5\pi/8, 0)$ and $(r_2, \theta_2, \varphi_2) = (1.146, 5\pi/8, 0)$.

in the literature for this problem (see [7] for instance). The computation of MRW branches is important because they give rise to three-frequency solutions [30], which are the last stage in the route to turbulence [54].

Quasiperiodic MRW are easily identified because their azimuthally-averaged properties are periodic, i.e, one frequency corresponds to the azimuthal drift of the wave and the other to the modulation. However, in some situations the modulation frequency could undergo period doubling bifurcations (see [55] for instance) making it difficult to identify the quasiperiodic character of the solution, even with the help of a frequency spectrum. For a better classification, Poincaré sections provide additional information. By means of Poincaré sections, periodic orbits are represented by a single point and quasiperiodic solutions as a closed curve, with loops if a period doubling bifurcation has occurred [55]. The Poincaré sections of the MRW bifurcated from the $m = 3$ RW branch at $\text{Ha} = 3.95$ and the MRW bifurcated from the $m = 4$ RW branch at $\text{Ha} = 31.95$, characteristic of the radial jet and return flow instability, respectively, are plotted in Fig. 11(a) and (b), respectively. The sections are defined by means of the radial velocity $v_r(r_s, \theta_s, \varphi_s) = 0$, where $(r_s, \theta_s, \varphi_s) = (1.5, 3\pi/4, 0)$ is a point in the middle of the shell at mid latitudes. On both panels the horizontal axis represents $v_r(1.5, 5\pi/8, 0)$ and the vertical axis $v_r(1.146, 5\pi/8, 0)$. On Fig. 11(a) the point represents a stable RW at $\text{Ha} = 4.19$. Because the bifurcation is subcritical, by de-

creasing Ha , a branch of MRW with azimuthal symmetry $m = 1$ is found. The two closed curves of Fig. 11(a) are representative of solutions belonging to this branch. The inner curve corresponds to $Ha = 3.80$ and the outer to $Ha = 3.54$. Analogously in Fig. 11(b) the two closed curves are MRW, but in this case the region of stability is smaller. The point corresponds to $Ha = 31.9$, the inner curve to $Ha = 32$ and the outer to $Ha = 32.02$.

5 Summary

The present analysis constitutes a further step towards a better understanding of the weakly nonlinear regime of the axially magnetised spherical Couette problem by extending previous studies [7, 43, 25] based on very few nonlinear solutions and on sketches of bifurcation diagrams. Our study represents the first application of Newton-Krylov continuation and stability analysis of the solutions to the MSC problem. For such high dimensional systems, modelling three-dimensional flows, there exist very few studies based on continuation methods, even in the more general context of fluid dynamics [28, 35].

Thanks to the use of continuation techniques a large number of nonlinear rotating waves have been obtained and the stability of around one third of the solutions have been established in a parameter regime of experimental interest, i.e Reynolds number $Re = 10^3$, aspect ratio $\eta = 0.5$ and Hartmann numbers $Ha \in (0, 80)$ corresponding to the working conditions of the HEDGEHOG experimental device at the Helmholtz-Zentrum Dresden-Rossendorf [9]. In this regime radial jet, return flow and shear-layer instabilities have been previously described [43, 25].

For a fixed Reynolds number we have accurately determined several regions of multistability and several transitions to quasiperiodic flows (modulated waves) of the first nonaxisymmetric instabilities with azimuthal wave numbers $m = 2, 3, 4$ that occur when the Hartmann number is varied. The symmetries of the bifurcated MRWs are identified and some examples are provided. The RW and their eigenfunctions at the bifurcation points provide initial conditions for the continuation of MRW that could be performed as in [30].

The patterns, rotation frequencies (i.e time scales) and some physical properties (nonaxisymmetric kinetic energy, for instance) of the radial jet, return flow and shear-layer instabilities have been exhaustively described in the range of $Ha \in (0, 80)$. For each azimuthal wave number the return flow instability changes continuously with increasing Ha to become the shear-layer instability. Both instabilities belong to the same branch. At the boundary between both instabilities, defined by a critical Ha , the nonaxisymmetric part of the flow is maximum. Nonaxisymmetry increases with decreasing wave number m . The critical Ha where nonaxisymmetric flow is

maximum increases with decreasing m , as well.

The determination of stability regions is crucial for comparison with experiments. They allow, for instance, to determine the azimuthal wave number of the most physically realisable solutions and thus help to design appropriate measurement set-ups. The azimuthal wave numbers of the branches chosen for this study matches with those that can be measured in the experiments [9]. The analysis of physical properties, such as the volume-averaged kinetic energies, serves as a prior estimate of their experimental values and thus as a guide for tuning measurement techniques. Once the solutions are obtained with continuation methods they can later be easily processed to obtain other measurable properties not shown in this study, for instance local velocities inside the shell or the torque acting on the outer sphere, for a further comparison with experiments.

6 Acknowledgements

F. Garcia was supported by a postdoctoral fellowship of the Alexander von Humboldt Foundation hosted by Helmholtz-Zentrum Dresden-Rossendorf. The authors thank the anonymous reviewers for constructive comments.

References

- [1] Larmor J, 1919 How could a rotating body such as the sun become a magnet? *Rep. Brit. Assoc. Adv. Sci.* 159–160
- [2] Gailitis A, Lielausis O, Platacis E, Gerbeth G, Stefani F, 2002 Magnetic field saturation in the Riga dynamo experiment. *Rev. Mod. Phys.* **74**, 973–990
- [3] Brandenburg A, Subramanian K, 2005 Astrophysical magnetic fields and nonlinear dynamo theory. *Phys. rep.* **417**
- [4] Dormy E, Soward AM, eds., 2007 *Mathematical Aspects of Natural Dynamos*, vol. 13 of *The Fluid Mechanics of Astrophysics and Geophysics*. Chapman & Hall/CRC
- [5] Peralta C, Melatos A, Giacobello M, Ooi A, 2006 Gravitational radiation from nonaxisymmetric spherical Couette flow in a neutron star. *Astrophys. J.* **644**, 53–56
- [6] Sisan DR, Mujica N, Tillotson WA, Huang YM, Dorland W, Hassam AB, Antonsen TM, Lathrop DP, 2004 Experimental observation and characterization of the magnetorotational instability. *Phys. Rev. Lett.* **93**, 114502

- [7] Hollerbach R, 2009 Non-axisymmetric instabilities in magnetic spherical Couette flow. *Proc. Roy. Soc. Lond. A* **465**, 2003–2013
- [8] Gissinger C, Ji H, Goodman J, 2011 Instabilities in magnetized spherical Couette flow. *Phys. Rev. E* **84**, 026308
- [9] Kasprzyk C, Kaplan E, Seilmayer M, Stefani F, 2017 Transitions in a magnetized quasi-laminar spherical Couette flow. *Magnetohydrodynamics* **53**, 393–401
- [10] Balbus SA, Hawley JF, 1991 A powerful local shear instability in weakly magnetized disks. i- Linear analysis. ii- Nonlinear evolution. *Astrophys. J.* **376**, 214–233
- [11] Ji H, Balbus S, 2013 Angular momentum transport in astrophysics and in the lab. *Phys. Today* **66**, 27–33
- [12] Stefani F, Gundrum T, Gerbeth G, Rüdiger G, Schultz M, Szklarski J, Hollerbach R, 2006 Experimental evidence for magnetorotational instability in a Taylor-Couette flow under the influence of a helical magnetic field. *Phys. Rev. Lett.* **97**, 184502
- [13] Stefani F, Gerbeth G, Gundrum T, Hollerbach R, Priede J, Rüdiger G, Szklarski J, 2009 Helical magnetorotational instability in a Taylor-Couette flow with strongly reduced Ekman pumping. *Phys. Rev. E* **80**, 066303
- [14] Seilmayer M, Galindo V, Gerbeth G, Gundrum T, Stefani F, Gellert M, Rüdiger G, Schultz M, Hollerbach R, 2014 Experimental evidence for nonaxisymmetric magnetorotational instability in a rotating liquid metal exposed to an azimuthal magnetic field. *Phys. Rev. Lett.* **113**, 024505
- [15] Stewartson K, 1966 On almost rigid rotations. Part 2. *J. Fluid Mech.* **26**, 131–144
- [16] Nakabayashi K, Tsuchida Y, 1995 Flow-history effect on higher modes in the spherical Couette system. *J. Fluid Mech.* **295**, 43–60
- [17] Zimmerman DS, Triana SA, Lathrop DP, 2011 Bi-stability in turbulent, rotating spherical Couette flow. *Phys. Fluids* **23**, 065104
- [18] Munson BR, Joseph DD, 1975 Viscous incompressible flow between concentric rotating spheres. Part 3. Linear stability. *J. Fluid Mech.* **69**, 705–719
- [19] Zikanov OY, 1996 Symmetry-breaking bifurcations in spherical Couette flow. *J. Fluid Mech.* **310**, 293–324

- [20] Hollerbach R, Junk M, Egbers C, 2006 Non-axisymmetric instabilities in basic state spherical Couette flow. *Fluid Dyn. Res.* **38**, 257–273
- [21] Schrauf G, 1986 The first instability in spherical Taylor-Couette flow. *J. Fluid Mech.* **166**, 287–303
- [22] Mamun CK, Tuckerman LS, 1995 Asymmetry and Hopf bifurcation in spherical Couette flow. *Phys. Fluids* **7**, 80–91
- [23] Hollerbach R, Skinner S, 2001 Instabilities of magnetically induced shear layers and jets. *Proc. Roy. Soc. Lond. A* **457**, 785–802
- [24] Figueroa A, Schaeffer N, Nataf HC, Schmitt D, 2013 Modes and instabilities in magnetized spherical Couette flow. *J. Fluid Mech.* **716**, 445–469
- [25] Kaplan EJ, 2014 Saturation of nonaxisymmetric instabilities of magnetized spherical Couette flow. *Phys. Rev. E* **85**, 1–8
- [26] Wei X, Hollerbach R, 2010 Magnetic spherical Couette flow in linear combinations of axial and dipolar fields. *Acta Mech.* **215**, 1–8
- [27] Kawahara G, Uhlmann M, van Veen L, 2012 The significance of simple invariant solutions in turbulent flows. *Arch. Ration. Mech. An.* **44**, 203–225
- [28] Dijkstra HA, *et al.*, 2014 Numerical bifurcation methods and their application to fluid dynamics: Analysis beyond simulation. *Commun. Comput. Phys.* **15**, 1–45
- [29] Viswanath D, 2007 Recurrent motions within plane Couette turbulence. *J. Fluid Mech.* **580**, 339–358
- [30] Garcia F, Net M, Sánchez J, 2016 Continuation and stability of convective modulated rotating waves in spherical shells. *Phys. Rev. E* **93**, 13119(11)
- [31] Sánchez J, Net M, Simó C, 2010 Computation of invariant tori by Newton-Krylov methods in large-scale dissipative systems. *Physica D* **239**, 123–133
- [32] van Veen L, Kawahara G, Atsushi M, 2011 On matrix-free computation of 2D unstable manifolds. *SIAM J. Sci. Comput.* **33**
- [33] Keller HB, 1977 Numerical solution of bifurcation and nonlinear eigenvalue problems. In PH Rabinowitz, ed., *Applications of Bifurcation Theory*, 359–384. Academic Press

- [34] Sánchez J, Garcia F, Net M, 2013 Computation of azimuthal waves and their stability in thermal convection in rotating spherical shells with application to the study of a double-Hopf bifurcation. *Phys. Rev. E* **87**, 033014/ 1–11
- [35] Sánchez J, Net M, 2016 Numerical continuation methods for large-scale dissipative dynamical systems. *Eur. Phys. J. Spec. Top.* **225**, 2465–2486
- [36] Golubitsky M, Stewart I, 2003 *The symmetry perspective: From equilibrium to chaos in phase space and physical space*. Basel: Birkhäuser
- [37] Rand D, 1982 Dynamics and symmetry. Predictions for modulated waves in rotating fluids. *Arch. Ration. Mech. An.* **79**, 1–37
- [38] Golubitsky M, LeBlanc VG, Melbourne I, 2000 Hopf bifurcation from rotating waves and patterns in physical space. *J. Nonlinear Sci.* **10**, 69–101
- [39] Andereck C, Liu S, Swinney H, 1986 Flow regimes in a circular Couette system with independently rotating cylinders. *J. Fluid Mech.* **164**, 155–183
- [40] Schaeffer N, Cardin P, 2005 Quasigeostrophic model of the instabilities of the Stewartson layer. *Phys. Fluids* **17**, 104111
- [41] Kuznetsov YA, 1998 *Elements of Applied Bifurcation Theory, Second Edition*. Springer
- [42] Schmitt D, Alboussière T, Brito D, Cardin P, Gagnière N, Jault D, Nataf HC, 2008 Rotating spherical Couette flow in a dipolar magnetic field: experimental study of magneto-inertial waves. *J. Fluid Mech.* **604**, 175–197
- [43] Travníkov V, Eckert K, Odenbach S, 2011 Influence of an axial magnetic field on the stability of spherical Couette flows with different gap widths. *Acta Mech.* **219**, 255–268
- [44] Garcia F, Net M, García-Archilla B, Sánchez J, 2010 A comparison of high-order time integrators for thermal convection in rotating spherical shells. *J. Comput. Phys.* **229**, 7997–8010
- [45] Frigo M, Johnson SG, 2005 The design and implementation of FFTW3. *Proceedings of the IEEE* **93**, 216–231. Special issue on "Program Generation, Optimization, and Platform Adaptation"
- [46] Goto K, van de Geijn RA, 2008 Anatomy of high-performance matrix multiplication. *ACM Trans. Math. Softw.* **34**, 1–25

- [47] Saad Y, Schultz MH, 1986 GMRES: a generalized minimal residual algorithm for solving nonsymmetric linear systems. *SIAM J. Sci. Stat. Comput.* **7**, 865–869
- [48] Ecke RE, Zhong F, Knobloch E, 1992 Hopf bifurcation with broken reflection symmetry in rotating Rayleigh-Bénard convection. *Europhys. Lett.* **19**, 177–182
- [49] Tuckerman LS, Langham J, Willis A, 2019 *Order-of-Magnitude Speedup for Steady States and Traveling Waves via Stokes Preconditioning in Channelflow and Openpipeflow*, 3–31. Springer International Publishing
- [50] Sánchez J, Net M, García-Archilla B, Simó C, 2004 Newton-Krylov continuation of periodic orbits for Navier-Stokes flows. *J. Comput. Phys.* **201**, 13–33
- [51] Tuckerman LS, 2015 Laplacian preconditioning for the inverse Arnoldi method. *Commun. Comput. Phys.* **18**, 1336–1351
- [52] Sánchez J, Garcia F, Net M, 2016 Radial collocation methods for the onset of convection in rotating spheres. *J. Comput. Phys.* **308**, 273–288
- [53] Feudel F, Tuckerman LS, Zaks M, Hollerbach R, 2017 Hysteresis of dynamos in rotating spherical shell convection. *Phys. Rev. Fluids* **2**, 053902
- [54] Ruelle D, Takens F, 1971 On the nature of turbulence. *Comm. in Math. Physics* **20**, 167
- [55] Garcia F, Sánchez J, Dormy E, Net M, 2015 Oscillatory convection in rotating spherical shells: Low Prandtl number and non-slip boundary conditions. *SIAM J. Appl. Dynam. Systems* **14**, 1787–1807